PHOTONICS Research

Fundamental limits for transmission modulation in VO₂ metasurfaces

BOHAN LI,[1] ⓘ ROCIO CAMACHO-MORALES,[1] ⓘ NEUTON LI,[1] ⓘ ANDREA TOGNAZZI,[2,3] ⓘ MARCO GANDOLFI,[3,4] ⓘ DOMENICO DE CEGLIA,[3,4] COSTANTINO DE ANGELIS,[3,4] ⓘ ANDREY A. SUKHORUKOV,[1] ⓘ AND DRAGOMIR N. NESHEV[1,*] ⓘ

[1]*ARC Centre of Excellence for Transformative Meta-Optical Systems (TMOS), Department of Electronic Materials Engineering, Research School of Physics, The Australian National University, Canberra, ACT 2601, Australia*
[2]*Department of Engineering, University of Palermo, Palermo 90128, Italy*
[3]*Istituto Nazionale di Ottica, Consiglio Nazionale delle Ricerche, Brescia 25123, Italy*
[4]*Department of Information Engineering, University of Brescia, Brescia 25123, Italy*
*Corresponding author: dragomir.neshev@anu.edu.au

The interest in dynamic modulation of light by ultra-thin materials exhibiting insulator–metal phase transition, such as VO₂, has rapidly grown due to the myriad industrial applications, including smart windows and optical limiters. However, for applications in the telecommunication spectral band, the light modulation through a thin VO₂ film is low due to the presence of strong material loss. Here, we demonstrate tailored nanostructuring of VO₂ to dramatically enhance its transmission modulation, reaching a value as high as 0.73, which is 2 times larger than the previous modulation achieved. The resulting designs, including free-topology optimization, demonstrate the fundamental limit in acquiring the desired optical performance, including achieving positive or negative transmission contrast. Our results on nanophotonic management of lossy nanostructured films open new opportunities for applications of VO₂ metasurfaces.   © 2022 Chinese Laser Press

https://doi.org/10.1364/PRJ.474328

1. INTRODUCTION

The rapidly growing scientific field of nano-optics paves the way for a variety of applications, including light manipulation [1,2], displays [3], sensing [4,5], and quantum technologies [6]. Using nanostructured materials, such as optical metasurfaces, one can outperform the functionalities of traditional bulk optics and further enable miniaturized optical systems and component integration. However, a broad range of nano-optical systems based at plasmonic [7] and dielectric [8,9] materials are static, and their optical properties remain fixed once the fabrication process is completed. Such static properties pose constraints to those applications where dynamic tunability of the optical elements is essential, such as displays and optical modulators.

Introducing dynamic tunability into post-fabricated systems relies on incorporating reconfigurable mechanisms [10], such as thermal [11–13], electrical [14,15], magnetic [16], and mechanical [17] methods. In the majority of mechanisms, the tunability is realized by modifying the optical refractive index $\tilde{n} = n + i\kappa$. However, the perturbation on $\tilde{n}$ is usually small [18–20], leaving a limited optical tuning performance or a narrow bandwidth operation [19]. On the contrary, the materials

with insulator–metal phase transition, such as vanadium dioxide (VO₂) [21,22], stand out due to the large index modulation across its insulating–metallic phase transition [23–26]. This phase transition of VO₂ occurs at ~68°C and can be thermally triggered. Alongside the phase transition, the refractive index values can change several orders of magnitude more than when using other reconfigurable mechanisms. Furthermore, the transition can repeatedly occur on a short time scale [27], which opens a wide potential in tunable nano-optics.

One of the fundamental phenomena in reconfigurable nanophotonics is transmission modulation, which finds important applications in optical switches, smart filters, and optical power limiters. The working principle of a VO₂ transmission modulator is based on the modulation of the material loss. At room temperatures, the VO₂ is in an insulator phase and exhibits low losses. Above the insulator–metal transition temperature, the material losses dramatically increase [23,24,26], and the transmissions are strongly damped, as shown in Fig. 1(a). As a result, the temperature control on VO₂ material enables a change in transmission efficiencies, defined by the transmission contrast $\Delta T = T_i - T_m$, where $T_{i,m}$ is the transmission through the insulator and the metallic phase.
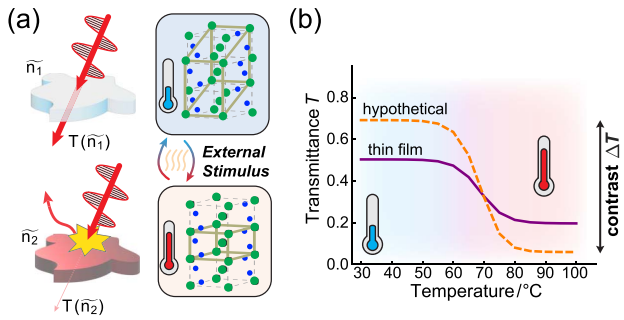
Fig. 1. (a) Schematic of the working principle of transmission modulation using insulator–metal phase transition in VO_2. The transmission efficiency T from the structure changes as the optical index of refraction varies with the phase transition. The crystalline structures of the low-temperature insulator phase and the high-temperature metallic phase are shown on the right-hand side [28]. The green spheres correspond to the vanadium atoms, and the blue spheres correspond to the oxygen atoms. (b) Enhancing the transmission contrast ΔT through nanostructuring. The hypothetical enhanced performance (orange curve) as compared to the transmission through an 80 nm VO_2 thin film on a silicon substrate (purple curve).

In previous works, the potential of VO_2 tunable transmission has been greatly explored [29,30]. However, most of the works focus on a much longer operating wavelength, where the losses of insulator VO_2 are not prominent. At the near-infrared spectral range and, more specifically, at around 1.55 μm, VO_2 exhibits large losses in both its insulator and metallic phases. With the excessive material loss, obtaining large transmission modulations using simple thin-film geometries is not trivial since the losses are too high to enable Fabry–Perot resonances. As a consequence, the maximally achievable transmission contrast through VO_2 thin-film structure is ~0.2 at the telecommunication wavelength around 1.55 μm [31,32].

One potential way to overcome this limit in thin-film geometries is to employ transverse nanostructuring, or more specifically, a periodic array of nanostructures (metasurface), where more complex electromagnetic responses can be introduced to help circumvent the detrimental losses of VO_2. This concept is illustrated in Fig. 1(b), which depicts the potential to tailor the transmission in both the VO_2 insulator and metallic states, allowing to increase in the transmission contrast. In recent years, there has been a growing interest in incorporating VO_2 into metasurfaces to achieve tunability, especially tunable Mie resonances [33–37]. However, most of the attention has been put onto the alternative aspects, such as reflection [38], Mie scattering cross section, or operation at longer mid-infrared wavelengths with reduced VO_2 loss. The actual transmission contrast at the telecommunication wavelength is still low, even though it can be 0.1–0.2 greater than the thin-film case. To date, it is not known what the maximally achievable modulation is and what the fundamental limits to the transmission contrast are.

Here, we demonstrate, theoretically, how through tailored design one can maximize the optical transmission modulation in VO_2 nanostructured films operating at telecommunication wavelengths. By nanostructuring the VO_2 thin film, we find

out that the transmission contrast can be tailored to be positive or negative, whereas the unpatterned films can only have positive values. More specifically, for operation at ~1.55 μm, we derive two different designs that can reach positive or negative transmission contrast roughly 2 times larger than what has been achieved with bare VO_2 film or other nanostructured films [33]. Our work provides deep insights into how to work with the optical losses of VO_2 to enhance transmission modulation. More practically, it opens up a wider possibility to enhance the transmission tunability of VO_2, which can be further translated into areas such as reflection, phase control, and polarization modulation.

2. RESULTS AND ANALYSIS

We first start by looking at a proof-of-concept geometry, a bare VO_2 thin film with a refractive index obtained from [26]. The transmission efficiency of the bare film can be calculated using the single-layer transfer matrix method [39]. Our calculations yield a maximum transmission contrast of 0.26 for a 210 nm thick VO_2 film [see Fig. 2(b)]. This value sets the performance benchmark of VO_2 for an incident wavelength of 1.55 μm.

In order to enhance the achievable transmission contrast, one can employ a periodic array of nanostructures to form a metasurface. A free-standing single-layer metasurface can be regarded as a layer of homogeneous material and characterized by its effective properties, including the effective dielectric constant ε_{eff} and magnetic permeability μ_{eff}, or equivalently the index of refraction $\tilde{n}_{\text{eff}}$ and material impedance z_{eff}. Based on these optical parameters, the reflectivity and transmissivity (i.e., the scattering coefficients) can be formulated as [40,41]

$$r = \frac{R_0(1 - e^{2i\tilde{\phi}})}{1 - R_0^2 e^{2i\tilde{\phi}}}, \tag{1}$$

$$t = \frac{(1 - R_0^2)e^{i\tilde{\phi}}}{1 - R_0^2 e^{2i\tilde{\phi}}}, \tag{2}$$

where $R_0 = \frac{z_{\text{eff}} - 1}{z_{\text{eff}} + 1}$ is the interface reflection, $\tilde{\phi} = k_0 h \tilde{n}_{\text{eff}}$ is the complex phase accumulated inside the layer, in which k_0 is the free space wave vector, and h is the thickness of the nanostructured layer. The phase term can be further decomposed based on the real and imaginary parts of the refractive index: $\tilde{\phi} = \phi_n + i\phi_\kappa = k_0 h(n_{\text{eff}} + i\kappa_{\text{eff}})$. The reflection and transmission efficiencies (R, T) can therefore be obtained by taking the modulus square of r and t. The absorption can also be calculated as $A = 1 - T - R$. For a high transmission efficiency $T \to 1$, small values of ϕ_κ are required. Therefore, besides reducing the structure thickness, for lossy materials, the nontrivial way to enhance the transmission is to reduce the effective extinction ratio κ_{eff}. On the other hand, low transmission efficiency $T \to 0$ can be achieved in multiple manners. For instance, the presence of high material loss already gives a low transmission provided by the large exponential damping factor. One can further decrease the transmission efficiency by implementing resonant absorption, thus obtaining even larger effective extinction ratios. Finally, the transmission can also be low when the interface reflection R_0 is high. To fulfill the desired
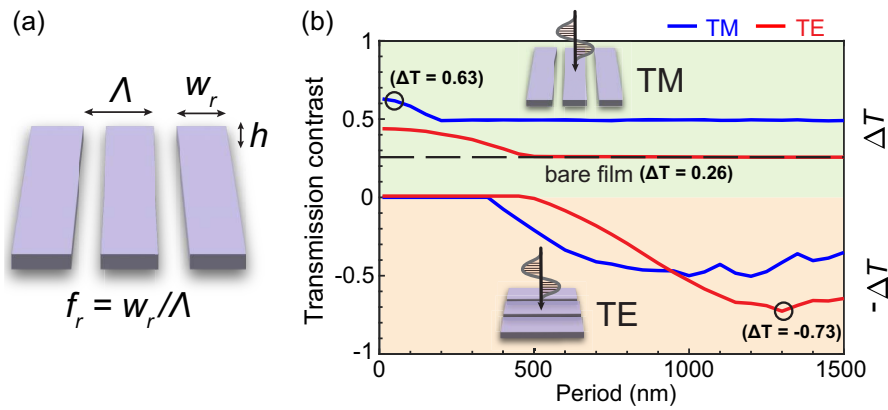
Fig. 2. (a) Schematic diagram of the metagrating studied in the parameter sweep. The incident wavelength is set to 1.55 μm, and the geometrical parameters include the grating height h, period Λ, filling ratio $f_r = w_r/\Lambda$, and polarization. (b) The maximally positive (green shaded) and negative (orange shaded) contrast ΔT over the period for different polarization conditions (blue for TM polarization, red for TE polarization). Two high-contrast regimes can be recognized and highlighted by the circles. The first regime has a positive contrast $\Delta T = 0.63$ with a deep-subwavelength periodicity ($\Lambda \ll \lambda$), while the second regime has a negative contrast $\Delta T = -0.73$ with a period close to the wavelength ($\Lambda \sim \lambda$). For comparison, the best performance of the bare VO_2 film is also shown with a constant value of 0.26 (black dashed line).

transmission performances, it is necessary to obtain specific values of the effective parameters; however, the exact means of how to achieve them remains unclear. The nanostructures can tune the effective parameters in a certain range based on the intrinsic properties of the composite materials, which is known as interpolation rules or mixing rules [42]. However, the interpolation functions are structure sensitive and nontrivial, which cannot be easily quantified. For this purpose, numerical optimization can be implemented to discover a design with the desired performance.

To identify some initial geometries with high transmission contrast, we first conducted a parameter sweep based on the free-standing subwavelength gratings with varying geometrical parameters. In particular, we calculated the transmission efficiency at normal incidence of a VO_2 grating in its insulator and metallic states, using rigorous coupled-wave analysis [43]. We varied the grating height, h, periodicity, Λ, filling ratio, f_r (defined as the ratio of the grating ridge width, w_r to the periodicity, i.e., $f_r = w_r/\Lambda$), and the polarization state of the incident light (TE or TM for electric field parallel or perpendicular to the grating ridges, respectively); see the schematic diagram in Fig. 2(a). The result of the parameter sweep is presented in Fig. 2(b). In particular, each point conforming the red and blue curves represents the largest magnitude of the transmission contrast, ΔT, which is achieved among all the possible grating geometries subject to the periodicity and polarization indicated in Fig. 2(b). From the parameter sweep, two prominent high-contrast regimes can be recognized, which are highlighted by the circles, with structure periodicity far less than the wavelength ($\Lambda \ll \lambda$) and period comparable to the wavelength ($\Lambda \sim \lambda$). The corresponding maximal transmission contrasts are given by 0.63 (positive ΔT, obtained for the TM mode) and -0.72 (negative contrast, achieved for the TE mode). Both of these maxima are more than 2 times greater than the maximum ΔT in the benchmark case with a bare VO_2 film. Here, the notation "positive" means $\Delta T = T_i - T_m > 0$ with a high transmission in the insulator

state and a low transmission in the metallic state, which is highlighted in Fig. 2(b) by the green shade, while "negative" means the opposite and is highlighted by the yellow shade. In the following sections, we will reveal the underlying physics of these two regimes respectively.

A. Achieving Positive Contrast in the Effective Medium Regime

As indicated in Fig. 2(b), the largest positive transmission contrast is achieved for a VO_2 grating with deep-subwavelength periodicity, i.e., $\Lambda \ll \lambda$. As shown by the upper blue line, when we proportionally scale down the transverse dimensions towards zero, while keeping the relative geometrical parameters (f_r) unchanged, the curve asymptotically approaches the maximum $\Delta T \to 0.63$. From practical considerations, we study the case of a grating having 50 nm periodicity. The corresponding transmission efficiencies in the insulator and metallic phases, together with the transmission contrast, are plotted in Fig. 3. Figures 3(a) and 3(b) show the dependence of the transmission with the grating geometry parameters, f_r and h, for the insulator and metallic phases of VO_2. The two VO_2 phases show similar oscillating behavior with respect to the thickness h, with the high transmission ridges in T_i highlighted by the black dashed lines. This oscillation means that the system behaves similarly to a VO_2 bare film with transmission sensitive to the longitudinal dimension. Due to the refractive index differences in the two VO_2 phases, the actual transmission responses are different, characterized by the magnitude of oscillation and the range of high transmission (denoted by yellow color). The maximum transmission contrast is obtained when the response of the two phases deviates the most, which is highlighted by the red star in Fig. 3(c).

In order to further understand the physical mechanism behind this high transmission contrast, in Fig. 4, we study the detailed electromagnetic responses of this optimal geometry when $\Delta T \to 0.63$. The corresponding grating parameters are $\Lambda = 50$ nm, $f_r = w_r/\Lambda = 0.83$, $h = 370$ nm, and TM
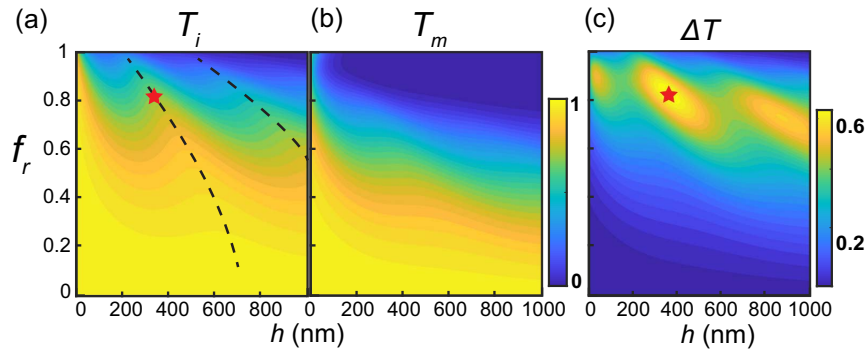
Fig. 3. Sweep of geometric parameters f_r and h in a grating structure with periodicity $\Lambda = 50$ nm, incident wavelength $\lambda = 1.55$ μm, and TM incident polarization. The 2D plots display the transmission efficiency of the VO$_2$ grating in the (a) insulating T_i and (b) metallic T_m phase of VO$_2$. The high transmission ridges in T_i are highlighted using black dashed lines. The transmission contrast ΔT of the grating is shown in (c). The optimal geometry with maximum contrast is highlighted by the red star with $f_r = 0.83$ and $h = 370$ nm.
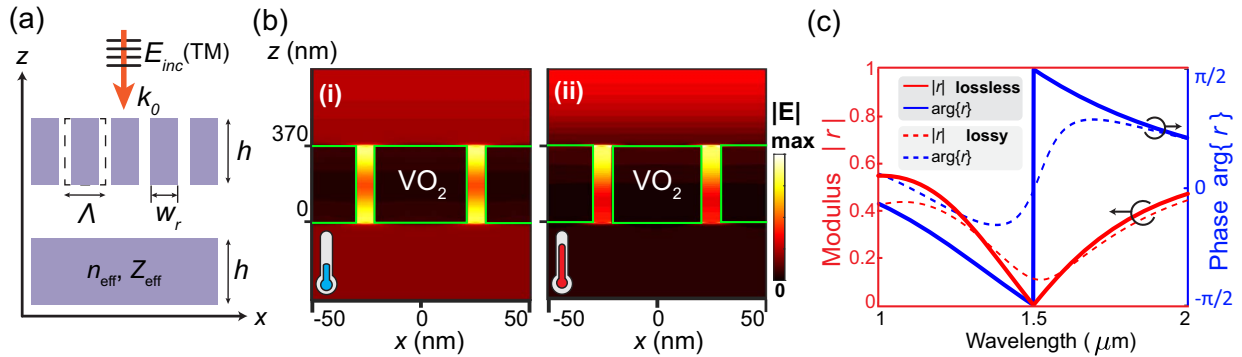
Fig. 4. (a) Schematic of the investigated structure (top) and comparison with the geometry in the effective medium regime (bottom). (b) Electric field amplitude distributions of the corresponding subwavelength grating at 1.55 μm, in the insulator (i) and metallic (ii) VO$_2$ states. (c) Reflectivity spectrum of the corresponding grating, where the amplitude $|r|$ and phase $\arg\{r\}$ are displayed by red and blue curves, respectively. The solid line denotes the lossless case with VO$_2$ material losses fully turned off, while the dashed line denotes the lossy case when the losses of the VO$_2$ material are considered.

polarization incidence (input electric field perpendicular to the grating ridges); see Fig. 4(a). We calculated the associated electromagnetic field profiles, shown in Fig. 4(b). When the VO$_2$ is in its lower loss insulator phase [region (i) in Fig. 4(b)], the electric field magnitude shows a symmetric distribution along the z direction, which results from Fabry–Perot (FP) interface reflections. In contrast, the FP oscillations are highly damped in the VO$_2$ metallic state, resulting in asymmetric field distribution in the z direction, as seen in region (ii) in Fig. 4(b). The longitudinal FP resonance for the dielectric VO$_2$ case can be more clearly seen in the reflectivity spectrum when the loss is set to zero, which is presented in Fig. 4(c). As shown by the solid lines representing the lossless case, a sharp dip in the amplitude of the reflectivity r is observed at ~1.5 μm (red line) alongside with a π phase shift at the same spectral location (blue line). Moreover, by retrieving the effective index of refraction, a 2π phase accumulation is obtained for each round trip inside the effective single-layer cavity. By adding the extra π phase shift from the Fresnel reflection at the first interface, the multiple reflected waves from the two interfaces interfere destructively, forming a transmissive FP cavity. When the extinction of VO$_2$ is included, the features of FP resonance

persist, indicated by a dip in reflectivity at 1.55 μm (red dashed line) and a more gradual electric field phase change (blue dashed line).

In addition, according to the extracted effective index of refraction, the effective extinction ratio of the VO$_2$ grating in the insulator state is significantly reduced, indicating suppression of the effective material loss. This can be attributed to the grating geometry itself, where the main effect comes from the thin air gaps between grating ridges. According to the electromagnetic field profile [Fig. 4(b)], the field is prominently concentrated inside the gap with minimal leakage into the VO$_2$ part outlined by the green color. The field concentration is essentially provided by the electromagnetic boundary condition and also the TM polarization state. Specifically, the normal component of the electric field displacement needs to be continuous, resulting in a significantly larger field magnitude inside the low-index air gap. This allows the wave to pass through the structure efficiently by circumventing the necessity of traveling through the lossy components. While for the metallic phase, although the electric field is still concentrated inside the gaps just like in the insulator phase, the field magnitude decays along the z direction; see region (ii) in Fig. 4(b). Consequently, in

this case, the behavior of the grating is dominated by material absorption.

The operating principle of the high transmission contrast in the effective medium regime can therefore be summarized as follows. Microscopically, the grating geometries with thin air gap support the concentration of electric field inside the gaps, which reduces the propagation loss. From the macroscopic perspective, the grating geometry supports an effective index of refraction that operates near the transmission FP mode for the insulator state with suppressed reflection. These features are not presented in the metallic state.

B. Reaching the Fundamental Limit by 2D Nanostructuring

Next, we extend our considerations to two-dimensional (2D) geometries to explore further optimization of the transmission modulation. In the effective medium regime, since the structure dimensions are far smaller than the wavelength, the metasurface can be homogenized into a single layer characterized by one effective parameter solely (e.g., ε_{eff}). Under this quasi-static regime, nonmagnetic materials are unable to excite artificial magnetic response, and therefore $\mu_{eff} \to 1$. Based on ε_{eff}, other effective properties can be easily derived: $\tilde{n}_{eff} = \sqrt{\varepsilon_{eff}}$, $z_{eff} = 1/\tilde{n}_{eff}$. Another feature of the effective medium regime is that the field amplitude inside each individual structural component can be regarded as constant with negligible phase variation.

Here, based on the two features mentioned above, we propose a 2D model composed of four regions, where the model represents a single-layer metasurface in the effective medium regime. The schematic diagram can be found in Fig. 5(a), where region 1 is filled by material 1 with dielectric permittivity ε_1, while regions 2, 3, and 4 are filled by material 2 with ε_2. Here, we limit our consideration to nonmagnetic materials with $\mu_{1,2} = 1$. The incident plane wave illuminates at normal incidence, and the electric field is set to be polarized in the x direction. The resulting field amplitudes in the adjacent regions are interconnected by electromagnetic boundary conditions.

Starting from region 1 with electric field amplitude E_1, one can relate field amplitudes in other regions to E_1. However, this leaves region 4 ambiguous since the 2-4 and 3-4 boundary conditions give distinct field amplitudes for region 4. To resolve the ambiguity, we set E_4 as a linear mixing between E_2 and E_3:

$$E_4 = f_{mix}E_2 + (1 - f_{mix})E_3, \tag{3}$$

with mixing ratio f_{mix} that can take values between 0 and 1. Using the averaging formulae for the effective dielectric constant,

$$\varepsilon_{eff} = \frac{1}{\varepsilon_0}\frac{\langle D \rangle}{\langle E \rangle}, \tag{4}$$

one can obtain the effective dielectric constant of this prototypical model as

$$\varepsilon_{eff} = \varepsilon_2 \frac{(1 - b_1)\varepsilon_1 + b_1\varepsilon_2}{(1 - b_2)\varepsilon_2 + b_2\varepsilon_1}, \tag{5}$$

with $b_1 = f_y(1 - f_x f_{mix})$ and $b_2 = f_x[1 - f_y(1 - f_{mix})]$ being the generalized filling ratios, and f_x and f_y being the linear filling ratio in the x and y directions, as shown in the schematic of Fig. 5(a). In the special cases when $f_x, f_y = 0, 1$, the formulae converge to the standard effective medium theory (EMT) of 1D nanostructures [44], which is listed in Table 1.

Using Eq. (5) and substituting the VO$_2$ dielectric constant into the position of ε_1 and setting $\varepsilon_2 = 1$ (air), one can obtain the maximum transmission contrast over a range of structure thicknesses. To confirm that the 2D EMT is the fundamental upper bound, we compare this theoretical prediction with the free-form topology optimization (TO) [45]. The EMT is constrained only to regular geometries; however, exotic topologies may exist that can exceed this performance. With TO, an optimal and arbitrary 2D grating can be designed efficiently by employing adjoint simulations, which helps in determining the shape gradients using minimal simulation time. The results
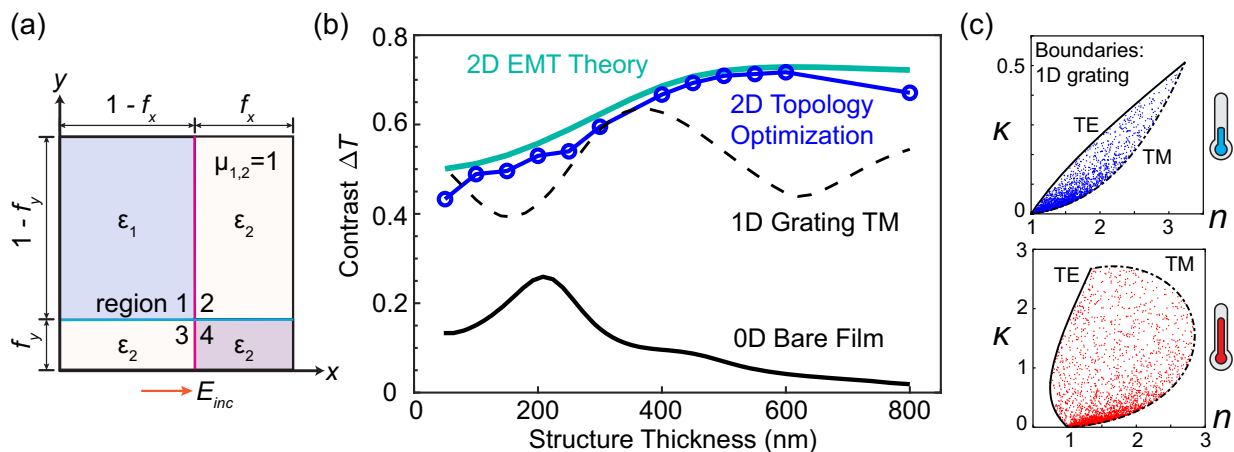
Fig. 5. (a) Diagram of the approximate zeroth-order effective medium theory (EMT). (b) Comparison between the predicted maximum ΔT using EMT (black solid curve), 1D grating with TM excitation (black dashed curve), unpatterned VO$_2$ film (black solid curve), and topology optimization (solid blue curve). The comparison shows the numerical optimization is well bounded by the theoretical prediction. (c) Effective index of refraction calculated with the EMT using random geometrical parameters. The results are shown by the distributed points, where the top and bottom n–κ maps correspond to the insulator and metallic phase of VO$_2$, respectively. The black edges correspond to the effective indices of the 1D grating geometries with TE or TM illumination.

Table 1. Effective Geometry and Dielectric Constant in the Cases with $f_{x,y} = 0$ or 1

Condition	Effective Structure	ε_{eff}
$f_x = 1$ or $f_y = 1$	Homogeneous layer	ε_2
$f_x = 0, f_y \neq 0$	1D grating TE incidence	$\varepsilon_{\text{eff}} = f_y \varepsilon_1 + (1 - f_y)\varepsilon_2$
$f_y = 0, f_x \neq 0$	1D grating TM incidence	$\varepsilon_{\text{eff}}^{-1} = f_x \varepsilon_1^{-1} + (1 - f_x)\varepsilon_2^{-1}$
$f_x = f_y = 0$	Homogeneous layer	ε_1

of TO are presented in Fig. 5(b) with the solid blue curve. From the comparison, the TO results are upper bounded by the EMT theoretical approximation given by Eq. (5), which shows the generality of this EMT model for single-layered metasurfaces within the deep-subwavelength regime. The discrepancy between numerical and theoretical calculations results from the finite resolution of the design space and the numerical inefficiency in searching for the global optimum. In Fig. 5(b), we also plot the simulation of a 1D grating with TM illumination [respective of Fig. 3(c), $f_r = 0.83$] and of a bare VO$_2$ film. Both of these results also remain well below the fundamental limit given by the EMT model.

The performance of the 2D model is generally much higher than that of the 1D grating or the bare VO$_2$ film. Comparing the global maximum contrast achieved in the different cases, we obtained $\max\{\Delta T\} \sim 0.26$ for a bare VO$_2$ film, $\max\{\Delta T\} \sim 0.63$ for a 1D grating, and $\max\{\Delta T\} \sim 0.73$ for 2D geometry. The maximum ΔT obtained in the 2D geometry is 16% greater than in the 1D case and 180% greater than that of the bare film. This extra enhancement can be understood using the effective index ($n - \kappa$) map, shown in Fig. 5(c), where the complex effective index ($\tilde{n}_{\text{eff}}$) of each geometry is denoted by a dot in the map. For the bare film, the refractive index is fixed to a dot, which can be regarded as a zero-dimensional object. For 1D structures, only a single line segment can be covered, whose path is determined by the grating interpolation rules as listed in Table 1. This produces a mismatch between the single geometrical parameter and the two degrees of freedom in the 2D $n - \kappa$ map spanned by the lossy VO$_2$ nanostructures. On the contrary, the 2D effective medium model can confidently span the whole 2D $n - \kappa$ space in between the boundaries generated by the 1D gratings [44], thereby providing a larger degree of freedom to tune the optical performances.

Importantly, the underlying physical mechanisms governing the high transmission contrast in 2D are similar to the 1D grating case. Despite the drastically various geometries obtained from topology optimization, the key feature is the presence of a narrow gap between adjacent structural elements. As an example, the geometries obtained by topology optimization are shown in Fig. 6(a), and the field profiles corresponding to the optimal structure are shown in Fig. 6(b). In the insulator state shown in panels (i) and (ii), the electric field is concentrated in the gap region, and the field profile shows a symmetry pattern along the longitudinal direction, indicating the presence of multiple reflections. As for the metallic state shown in panels (iii) and (iv), the behavior is dominated by absorption as the field magnitude decays along the longitudinal direction.
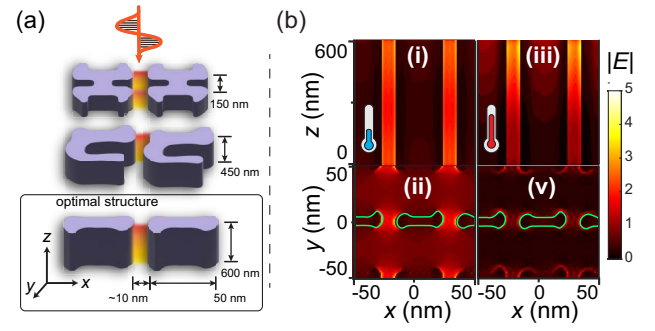

Fig. 6. (a) Optimal geometries obtained from topology optimization using different thicknesses of the VO$_2$ scattering structures. A common feature can be distinguished among all these geometries: the thin gap between adjacent structure elements is along the electric field direction. On the bottom, we report the geometry with the highest contrast $\Delta T = 0.73$, obtained for $h = 600$ nm, $\Lambda = 50$ nm, and incident wavelength $\lambda = 1.55$ μm, which is well within the deep-subwavelength regime. (b) Calculated electric field profiles of the optimal structure (i), (ii) in its insulator state, and (iii), (iv) in its metallic state. Calculations (i) and (iii) show the side view of the structure (perspective along the x axis) with the cut plane located at $y = 0$, while (ii) and (iv) show the bottom view (perspective along the z axis) with the cut plane located at $z = 0$. The green contour marks the structure's edges.

C. Achieving Negative Contrast in the Resonant Regime

This section discusses the second regime when the 1D metasurface period is comparable to the wavelength $\Lambda \sim \lambda$. The maximally negative contrast occurs at $\Lambda = 1300$ nm periodicity for the TE electric field. The associated result of parameter sweep is elaborated in Fig. 7.

Figure 7(a) presents the corresponding transmission efficiency of the grating in the insulating state (T_i). The transmission shows complex dependence over the grating geometrical parameters f_r and h, exhibiting a completely different behavior compared to the deep-subwavelength regime, as depicted in Fig. 3. In particular, the transmission efficiency is generally low, with several narrow valleys of near-zero transmission efficiency, which are highlighted by the white dashed curves. The transmission in the metallic state (T_m) shown in Fig. 7(b) is similar to what has been previously discussed, where the transmission reduces with larger filling ratios or larger thicknesses. Combining the responses of the two phases yields a negative transmission contrast as high as $\Delta T = -0.73$, which is denoted by the red star in the transmission contrast plot shown in Fig. 7(c).

The optimal geometry is given as a thin grating with a large period and TE polarization illumination. A detailed schematic diagram is shown in Fig. 8(a) with the specific geometrical parameters: $\Lambda = 1300$ nm, $h = 640$ nm, $f_r = 0.05$. Intuitively, the scattering cross section is low due to the small transverse filling ratio of the VO$_2$ grating, which should lead to a high transmission efficiency. While this is the case for the metallic state, giving $T_m \sim 0.74$, the actual transmission efficiency in the insulator state, however, is nearly eliminated, $T_i \sim 0.01$. This total extinction of far-field transmission has
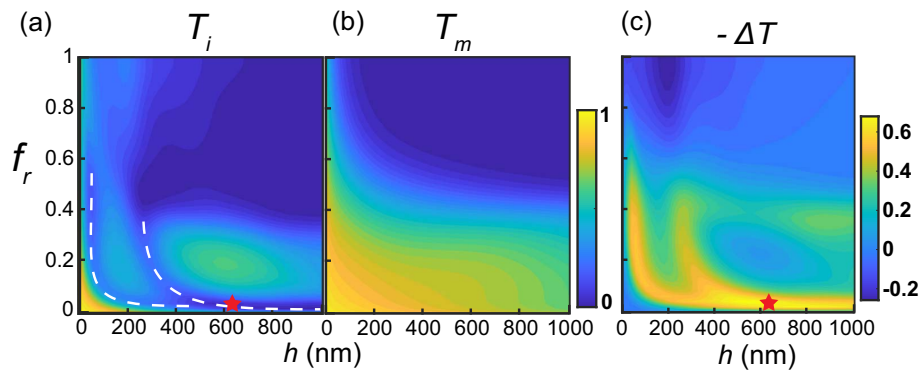
Fig. 7. Parameter sweep of geometric parameters f_r and h in a grating structure with periodicity $\Lambda = 1300$ nm, incident wavelength $\lambda = 1.55$ μm, and TE incident polarization. The 2D plots display the transmission efficiency of the VO$_2$ grating in the (a) insulating (T_i) and (b) metallic (T_m) phase. For T_i, the low transmission valleys are highlighted by the white dashed lines. The associated negative transmission contrast $-\Delta T$ is presented in (c). The red star highlights the optimal geometry with maximum negative transmission contrast for the parameters $h = 640$ nm and $f_r = 0.05$.

been previously reported in Ref. [46] with sparse and low-filling grating structure, where the mechanism is attributed to the multiple scattering effects. Here, we provide qualitative analysis to describe the underlying physics further.

By examining the electromagnetic field pattern of the insulator VO$_2$ grating, presented in Fig. 8(b), we found that the grating exerts a strong electric field amplitude and phase distortion. In particular, large electric field amplitude is seen at both the grating ridges as well as in the middle of the wide air gap, which agrees with the observation in Ref. [46]. The phase front is significantly bent, showing a strong influence on the flow of electromagnetic energy. On the contrary, the amplitude modulation is weaker for the metallic state shown in Fig. 8(c). In fact, the metallic VO$_2$ effectively repels the electric field, resulting in a lower field amplitude inside or near the grating rods. In addition, the phase front distortion effect is much weaker as compared to the insulating phase, and the wave generally keeps the forward propagating tendency. The net effect is a high transmission efficiency.

To further analyze this transmission suppression for the insulator VO$_2$ grating, we studied the associated reflection and
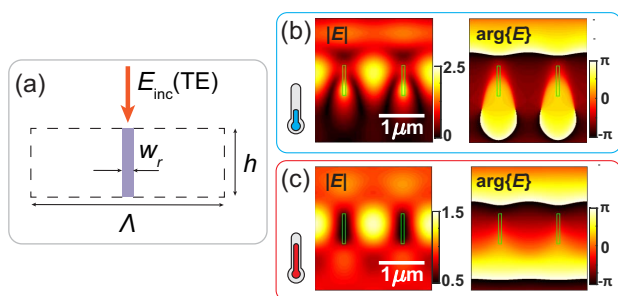

Fig. 8. (a) Schematic diagram of the design having maximally negative contrast at $\lambda = 1.55$ μm wavelength, with geometrical parameters $\Lambda = 1300$ nm, $f_r = 0.05$, and $h = 640$ nm. The structure is illuminated with TE polarization, i.e., an electric field parallel to the grating ridges. The calculated electric field amplitude and phase profiles of the corresponding structure in the insulator phase of VO$_2$ are shown in (b) and in the metallic phase of VO$_2$ in (c).

absorption spectrum, presented in Fig. 9(a). At the target wavelength $\lambda = 1.55$ μm, the spectrum exhibits a dip in transmission efficiency with ~80% of the energy being absorbed. Having an absorption higher than 50% indicates the excitation of more than one type of resonance [47]. Here we address the origin of these resonant features and provide a qualitative analysis of the observed behaviors.

The first resonance type is related to the periodic lattice structure, which can be studied more directly when the material loss is set to zero. In that case, a wide band transmission suppression is shown at the central wavelength of $\lambda \sim 1.45$ μm, as shown in Fig. 9(b). However, in this case, the dominant effect is the near-perfect reflection. To better analyze the origin of this behavior, we solve the optical problem with COMSOL Multiphysics for five individual rectangular rods separated by $\Lambda = 1300$ nm and surrounded by perfectly matched layers (PMLs). We then present the electric field magnitude together with the time-averaged Poynting vectors to visualize the energy flow direction. For the lossless scenario shown in Fig. 9(d), in the periodic regime at the middle, the Poynting vectors form vortices that cancel out with the adjacent ones, which indicates the presence of strong interference between the multiple scattered waves. In addition, the magnitudes of the vectors are generally small. Together with the alternately strong and weak electric field amplitude pattern shown in Fig. 9(d), it indicates the presence of a standing wave originating from the periodic lattice resonance. This standing wave feature can be more clearly visualized at the structure edges, where the lattice translation symmetry is broken. Indeed, at the edges, a strong transverse energy flow is presented in a symmetric manner against the center of the structure. These observations are consistent with the previous report on the wideband reflector, where the behavior is attributed to the in-plane Bloch mode [48].

When looking at the realistic lossy case, shown in Fig. 9(c), the wave behavior is drastically different, where the Poynting vectors tend to flow toward the grating ridges in both the periodic regime and also the edges. This concentration of energy flow originates from the scattering of the individual rectangular rod, whose electric field profile shows a similar pattern as
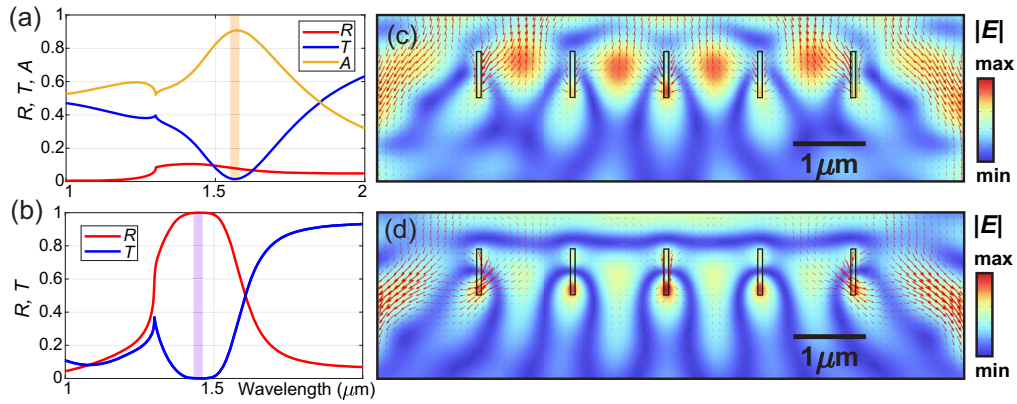
Fig. 9. (a), (b) Spectra and (c), (d) field patterns of the VO$_2$ grating in the insulator state. For the realistic lossy case given in (a), (c), a transmission suppression dip is shown in (a) centered at the target wavelength 1.55 μm. In panel (c), the corresponding electric field distribution (shown by the background density plot) and also the flow of Poynting vectors (red arrows) are displayed. The material loss is turned off for (b) and (d). In (b), the broadband transmission suppression is centered at 1.45 μm. The corresponding field pattern and Poynting vector flow are displayed in panel (d).
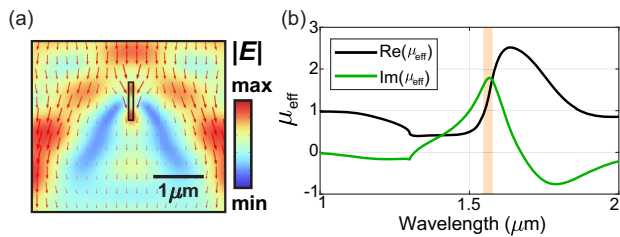
Fig. 10. (a) Calculated electromagnetic behavior of a single rectangular rod. In particular, it shows the amplitude of the electric field, as indicated by the color bar on the right, together with the flow of the Poynting vectors, as indicated by the red arrows. (b) The spectrum of the retrieved effective magnetic permeability (μ_{eff}). A peak is presented in the imaginary part at the wavelength of interest 1.55 μm.

indicated in Fig. 10(a), where the simulation is done with a single rod and PMLs. However, according to the field distribution and direction of the Poynting vectors in Fig. 10(a), the individual scatterers themselves cannot support the complete suppression of forward scattering, meaning that the near-zero transmission originates from a joint contribution of the scattering of individual scatterer as well as the periodic lattice geometry. Finally, by retrieving the effective magnetic permeability μ_{eff} based on the method in Ref. [40], we found that the imaginary part of μ_{eff} shows a peak at ~1.55 μm. These calculations, shown in Fig. 10(b), further validate the contribution from the magnetic-type resonance from the individual rectangular rod. Together with the grating lattice resonance, it gives a hyperabsorption effect with 80% absorption.

3. CONCLUSIONS

In this work, we study light modulation through nanostructured VO$_2$ films to optimize the transmission modulation performance and derive the fundamental limits of such switching. We show how the tailored nanostructuring of the films can engineer the interplay between absorption and scattering, thereby maximizing the transmission contrast. Through our studies,

we derive two fundamentally different optimized designs for tunable transmission through VO$_2$-based metasurfaces. Both designs exhibit a large magnitude of the transmission modulation depth at telecommunication wavelengths, however, with opposite signs. The achievable transmission contrast for both designs is $|\Delta T| \sim 0.73$, which is 2 times greater than what can be achieved by a bare VO$_2$ film and 2 times larger than what has been previously reported.

The first design is achieved within the deep-subwavelength regime for structure periodicity far less than the operating wavelength. The optimal geometry is given by a metasurface with periodically arranged cuboids or dumbbell-shaped meta-atoms derived from topology optimization. These structures essentially support a Fabry–Perot type of anti-reflection in the insulator state while exhibiting an absorptive nature in the metallic state, resulting in a high transmission contrast. The simulation results show transmission modulation that is upper limited by the 2D effective medium theory model, giving a full degree of freedom to modify the effective optical parameter for lossy nanostructures.

The second design results in a negative transmission modulation, which is impossible for thin-film geometry. It is given by a grating structure with a periodicity similar to the wavelength and operating in the resonant regime. The filling ratio of this structure is low, which automatically gives a high transmission in the metallic state for TE polarization. Instead, in the insulator state, the transmission is limited by resonant absorption, which originates from two different types of resonances, including a local resonance of the individual grating elements and a Bloch-type lattice resonance associated with the periodicity of the metasurface geometry.

These proposed designs provide a tunable transmission platform with a large modulation depth and incorporate all the advantages of VO$_2$, including a large bandwidth, fast modulation speed, and stability for repeated switching. Our results provide a deeper insight into the fundamental limitations of nanostructured VO$_2$ films and metasurfaces, as well as other nanostructured lossy materials, in achieving the desired optical performance with high-transmission contrast.

Disclosures. The authors declare no conflicts of interest.

Data Availability. Data underlying the results presented in this paper are not publicly available at this time but may be obtained from the authors upon reasonable request.

REFERENCES

1. C. Wan, Z. Zhang, J. Salman, J. King, Y. Xiao, Z. Yu, A. Shahsafi, R. Wambold, S. Ramanathan, and M. A. Kats, "Ultrathin broadband reflective optical limiter," Laser Photonics Rev. **15**, 2100001 (2021).
2. C. Wan, E. H. Horak, J. King, J. Salman, Z. Zhang, Y. Zhou, P. Roney, B. Gundlach, S. Ramanathan, R. H. Goldsmith, and M. A. Kats, "Limiting optical diodes enabled by the phase transition of vanadium dioxide," ACS Photonics **5**, 2688–2692 (2018).
3. O. Hemmatyar, S. Abdollahramezani, I. Zeimpekis, S. Lepeshov, A. Krasnok, A. I. Khan, K. M. Neilson, C. Teichrib, T. Brown, E. Pop, D. W. Hewak, M. Wuttig, A. Alu, O. L. Muskens, and A. Adibi, "Enhanced meta-displays using advanced phase-change materials," arXiv, arXiv:2107.12159 (2021).
4. B. I. Karawdeniya, A. M. Damry, K. Murugappan, S. Manjunath, Y. N. D. Bandara, C. J. Jackson, A. Tricoli, and D. Neshev, "Surface functionalization and texturing of optical metasurfaces for sensing applications," Chem. Rev. **122**, 14990–15030 (2022).
5. H. Altug, S.-H. Oh, S. A. Maier, and J. Homola, "Advances and applications of nanophotonic biosensors," Nat. Nanotechnol. **17**, 5–16 (2022).
6. K. Wang, J. G. Titchener, S. S. Kruk, L. Xu, H.-P. Chung, M. Parry, I. I. Kravchenko, Y.-H. Chen, A. S. Solntsev, Y. S. Kivshar, D. N. Neshev, and A. A. Sukhorukov, "Quantum metasurface for multiphoton interference and state reconstruction," Science **361**, 1104–1108 (2018).
7. J. Boken, P. Khurana, S. Thatai, D. Kumar, and S. Prasad, "Plasmonic nanoparticles and their analytical applications: a review," Appl. Spectrosc. Rev. **52**, 774–820 (2017).
8. A. Barreda, J. Saiz, F. González, F. Moreno, and P. Albella, "Recent advances in high refractive index dielectric nanoantennas: basics and applications," AIP Adv. **9**, 040701 (2019).
9. M. R. Hasan and O. G. Hellesø, "Dielectric optical nanoantennas," Nanotechnology **32**, 202001 (2021).
10. L. Carletti, M. Gandolfi, D. Rocco, A. Tognazzi, D. de Ceglia, M. A. Vincenti, and C. D. Angelis, "Reconfigurable nonlinear response of dielectric and semiconductor metasurfaces," Nanophotonics **10**, 4209–4221 (2021).
11. M. A. Kats, R. Blanchard, P. Genevet, Z. Yang, M. M. Qazilbash, D. Basov, S. Ramanathan, and F. Capasso, "Thermal tuning of mid-infrared plasmonic antenna arrays using a phase change material," Opt. Lett. **38**, 368–370 (2013).
12. M. Rahmani, L. Xu, A. E. Miroshnichenko, A. Komar, R. Camacho-Morales, H. Chen, Y. Zárate, S. Kruk, G. Zhang, D. N. Neshev, and Y. S. Kivshar, "Reversible thermal tuning of all-dielectric metasurfaces," Adv. Funct. Mater. **27**, 1700580 (2017).
13. D. Rocco, M. Gandolfi, A. Tognazzi, G. Zograf, K. Frizyuk, C. Gigli, G. Leo, S. Makarov, M. Petrov, and C. D. Angelis, "Opto-thermally controlled beam steering in nonlinear all-dielectric metastructures," Opt. Express **29**, 37128–37139 (2021).
14. Y. Zhang, C. Fowler, J. Liang, B. Azhar, M. Y. Shalaginov, S. Deckoff-Jones, S. An, J. B. Chou, C. M. Roberts, V. Liberman, M. Kang, C. Ríos, K. A. Richardson, C. Rivero-Baleine, T. Gu, H. Zhang, and J. Hu, "Electrically reconfigurable non-volatile metasurface using low-loss optical phase-change material," Nat. Nanotechnol. **16**, 661–666 (2021).
15. Y. Wang, P. Landreman, D. Schoen, K. Okabe, A. Marshall, U. Celano, H.-S. P. Wong, J. Park, and M. L. Brongersma, "Electrical tuning of phase-change antennas and metasurfaces," Nat. Nanotechnol. **16**, 667–672 (2021).
16. Y. V. Izdebskaya, Z. Yang, M. Liu, D.-Y. Choi, A. Komar, D. N. Neshev, and I. V. Shadrivov, "Magnetic tuning of liquid crystal dielectric metasurfaces," Nanophotonics **11**, 3895–3900 (2022).
17. E. Arbabi, A. Arbabi, S. M. Kamali, Y. Horie, M. Faraji-Dana, and A. Faraon, "Mems-tunable dielectric metasurface lens," Nat. Commun. **9**, 812 (2018).
18. J. Leuthold, C. Koos, and W. Freude, "Nonlinear silicon photonics," Nat. Photonics **4**, 535–544 (2010).
19. J. H. Vella, J. H. Goldsmith, A. T. Browning, N. I. Limberopoulos, I. Vitebskiy, E. Makri, and T. Kottos, "Experimental realization of a reflective optical limiter," Phys. Rev. Appl. **5**, 064010 (2016).
20. J. Li, S.-T. Wu, S. Brugioni, R. Meucci, and S. Faetti, "Infrared refractive indices of liquid crystals," J. Appl. Phys. **97**, 073501 (2005).
21. F. Morin, "Oxides which show a metal-to-insulator transition at the Neel temperature," Phys. Rev. Lett. **3**, 34–36 (1959).
22. J. B. Goodenough, "The two components of the crystallographic transition in VO_2," J. Solid State Chem. **3**, 490–500 (1971).
23. H. Kakiuchida, P. Jin, S. Nakao, and M. Tazawa, "Optical properties of vanadium dioxide film during semiconductive–metallic phase transition," Jpn. J. Appl. Phys. **46**, L113–L116 (2007).
24. M. Currie, M. A. Mastro, and V. D. Wheeler, "Characterizing the tunable refractive index of vanadium dioxide," Opt. Mater. Express **7**, 1697–1707 (2017).
25. S. Cueff, J. John, Z. Zhang, J. Parra, J. Sun, R. Orobtchouk, S. Ramanathan, and P. Sanchis, "VO_2 nanophotonics," APL Photonics **5**, 110901 (2020).
26. C. Wan, Z. Zhang, D. Woolf, C. M. Hessel, J. Rensberg, J. M. Hensley, Y. Xiao, A. Shahsafi, J. Salman, S. Richter, Y. Sun, M. M. Qazilbash, R. Schmidt-Grund, C. Ronning, S. Ramanathan, and M. A. Kats, "On the optical properties of thin-film vanadium dioxide from the visible to the far infrared," Ann. Phys. **531**, 1900188 (2019).
27. P. Markov, R. E. Marvel, H. J. Conley, K. J. Miller, R. F. Haglund, Jr., and S. M. Weiss, "Optically monitored electrical switching in VO_2," ACS Photonics **2**, 1175–1182 (2015).
28. A. Cavalleri, C. Tóth, C. W. Siders, J. Squier, F. Ráksi, P. Forget, and J. Kieffer, "Femtosecond structural dynamics in VO_2 during an ultrafast solid-solid phase transition," Phys. Rev. Lett. **87**, 237401 (2001).
29. M. Larciprete, M. Centini, S. Paoloni, I. Fratoddi, S. Dereshgi, K. Tang, J. Wu, and K. Aydin, "Adaptive tuning of infrared emission using VO_2 thin films," Sci. Rep. **10**, 11544 (2020).
30. T. Cesca, C. Scian, E. Petronijevic, G. Leahu, R. L. Voti, G. Cesarini, R. Macaluso, M. Mosca, C. Sibilia, and G. Mattei, "Correlation between in situ structural and optical characterization of the semiconductor-to-metal phase transition of VO_2 thin films on sapphire," Nanoscale **12**, 851–863 (2020).
31. D. U. Singh, O. Bhoite, and R. Narayanan, "Temperature tunable optical transmission using IR based 1D photonic crystals of VO_2 nanostructures," J. Phys. D **53**, 245106 (2020).
32. H. Kocer, A. Ozer, S. Butun, K. Wang, J. Wu, H. Kurt, and K. Aydin, "Thermally tuning infrared light scattering using planar layered thin films and space gradient metasurface," IEEE J. Sel. Top. Quantum Electron. **25**, 4700607 (2019).
33. A. Howes, Z. Zhu, D. Curie, J. R. Avila, V. D. Wheeler, R. F. Haglund, and J. G. Valentine, "Optical limiting based on Huygens-metasurfaces," Nano Lett. **20**, 4638–4644 (2020).
34. A. Tripathi, J. John, S. Kruk, Z. Zhang, H. S. Nguyen, L. Berguiga, P. R. Romeo, R. Orobtchouk, S. Ramanathan, Y. Kivshar, and S. Cueff, "Tunable Mie-resonant dielectric metasurfaces based on

VO₂ phase-transition materials," ACS Photonics **8**, 1206–1213 (2021).

35. N. A. Butakov, I. Valmianski, T. Lewi, C. Urban, Z. Ren, A. A. Mikhailovsky, S. D. Wilson, I. K. Schuller, and J. A. Schuller, "Switchable plasmonic–dielectric resonators with metal–insulator transitions," ACS Photonics **5**, 371–377 (2018).

36. T. Kang, B. Fan, J. Qin, W. Yang, S. Xia, Z. Peng, B. Liu, S. Peng, X. Liang, T. Tang, L. Deng, Y. Luo, H. Wang, Q. Zhou, and L. Bi, "Mid-infrared active metasurface based on Si/VO₂ hybrid meta-atoms," Photonics Res. **10**, 373–380 (2022).

37. P. Kepic, F. Ligmajer, M. Hrton, H. Ren, L. D. S. Menezes, S. A. Maier, and T. Sikola, "Optically tunable Mie resonance VO₂ nanoantennas for metasurfaces in the visible," ACS Photonics **8**, 1048–1057 (2021).

38. A. M. Boyce, J. W. Stewart, J. Avila, Q. Shen, S. Zhang, V. D. Wheeler, and M. H. Mikkelsen, "Actively tunable metasurfaces via plasmonic nanogap cavities with sub-10-nm VO₂ films," Nano Lett. **22**, 3525–3531 (2022).

39. P. Yeh, A. Yariv, and C.-S. Hong, "Electromagnetic propagation in periodic stratified media. I. General theory," J. Opt. Soc. Am. **67**, 423–438 (1977).

40. X. Chen, T. M. Grzegorczyk, B.-I. Wu, J. Pacheco, Jr., and J. A. Kong, "Robust method to retrieve the constitutive effective parameters of metamaterials," Phys. Rev. E **70**, 016608 (2004).

41. Z. Szabo, G.-H. Park, R. Hedge, and E.-P. Li, "A unique extraction of metamaterial parameters based on Kramers–Kronig relationship," IEEE Trans. Microw. Theory Tech. **58**, 2646–2653 (2010).

42. J. Rensberg, S. Zhang, Y. Zhou, A. S. McLeod, C. Schwarz, M. Goldflam, M. Liu, J. Kerbusch, R. Nawrodt, S. Ramanathan, D. N. Basov, F. Capasso, C. Ronning, and M. A. Kats, "Active optical metasurfaces based on defect-engineered phase-transition materials," Nano Lett. **16**, 1050–1055 (2016).

43. J. P. Hugonin and P. Lalanne, "Reticolo software for grating analysis," arXiv, arXiv:2101.00901 (2021).

44. D. Aspnes, "Bounds on allowed values of the effective dielectric function of two-component composites at finite frequencies," Phys. Rev. B **25**, 1358–1361 (1982).

45. S. Molesky, Z. Lin, A. Y. Piggott, W. Jin, J. Vucković, and A. W. Rodriguez, "Inverse design in nanophotonics," Nat. Photonics **12**, 659–670 (2018).

46. P. Ghenuche, G. Vincent, M. Laroche, N. Bardou, R. Hadar, J.-L. Pelouard, and S. Collin, "Optical extinction in a single layer of nanorods," Phys. Rev. Lett. **109**, 143903 (2012).

47. R. Alaee, M. Albooyeh, and C. Rockstuhl, "Theory of metasurface based perfect absorbers," J. Phys. D **50**, 503002 (2017).

48. Y. H. Ko and R. Magnusson, "Wideband dielectric metamaterial reflectors: Mie scattering or leaky Bloch mode resonance?" Optica **5**, 289–294 (2018).